Optical constants from scattering-type scanning near-field optical microscope

Xiao Guo, Karl Bertling, and Aleksandar D. Rakić

View Online   Export Citation   CrossMark
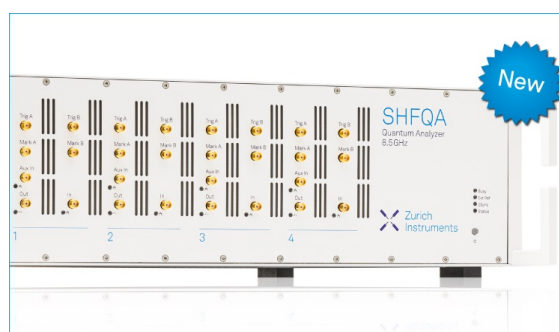
Optical constants from scattering-type scanning near-field optical microscope

View Online   Export Citation   CrossMark

Xiao Guo, (iD) Karl Bertling, (iD) and Aleksandar D. Rakić[a] (iD)

AFFILIATIONS

School of Information Technology and Electrical Engineering, The University of Queensland, Brisbane QLD 4072, Australia

[a]Author to whom correspondence should be addressed: a.rakic@uq.edu.au

ABSTRACT

Scattering-type scanning near-field optical microscopy (s-SNOM) allows for the characterization of optical properties of samples at the nanoscale, well below the diffraction limit of the interrogating wavelength. Typically, it relies on a model for the probe-sample interaction to extract complex optical constants of the sample. Here, we propose an s-SNOM calibration method that allows for the extraction of these constants without prior knowledge of the probe geometry nor the details of the probe-sample interactions. We illustrate the technique using terahertz time-domain spectroscopy-based s-SNOM to extract the optical properties of several organic and inorganic materials and differently doped regions of a standard silicon random access memory sample. The accuracy of the technique is comparable to that of conventional far-field techniques while additionally providing spatial distribution of optical constants at the nanoscale. The source-independent nature of the proposed technique makes it directly applicable for s-SNOM measurements in other spectral ranges.

Nanoscopy utilizing Scanning Near-field Optical Microscopes[1–3] is a valuable tool for investigating organic and inorganic materials on the nanoscale.[4–12] This is of particular interest in the mid-infrared (MIR) and terahertz (THz) regions of the spectrum where the long wavelengths (of tens to hundreds of μm with consequently large diffraction-limited spots) prevent the applicability of the conventional far-field characterization methods for investigation of micro- and nanoscale materials, structures, and features.

At these wavelengths, a slew of applications have emerged over the past few decades where scattering-type scanning near-field optical microscopy (s-SNOM) was identified as a useful tool for measuring optical properties of materials with the nanoscale spatial resolution.[13–17] These include (1) the identification of phonon resonances,[18,19] localized plasmonic resonances,[20] and free-carrier spatial and spectral profiles in the MIR[21,22] and THz[23,24] regimes while assuming the prior knowledge of the permittivity of the sample or (2) extracting the unknown sample permittivity in the vicinity of resonances.[25–29]

The amplitude and phase of the s-SNOM scattering signal contain the information about the optical constants of the sample material located underneath the probe. The key question still is how to effectively extract the optical constants of the sample from the measured s-SNOM signal. Models developed to describe the electromagnetic interaction between the probe-sample system and the incident electromagnetic wave include the widely used dipole models[30,31] and the

recent, state-of-the-art, numerical models.[27,32,33] These comprehensive models provide an improved physical understanding of the near-field probe-sample coupling, giving them a theoretical edge over the dipole model approximations. They properly identify the need for including the realistic shape of the probe to reproduce the measured scattering signal and relating the shape of the s-SNOM signal not only to the probe geometry but also to the tapping amplitude, minimum approach distance, and the spurious contributions from parts of the system other than the probe.[32]

On the other hand, the essence of the multiple interactions between the probe and the sample has been well captured by both the comprehensive models and the dipole model approximations. This difficult inverse problem is not only *ill-posed*[34] but is also compounded by the fact that, while the probe-sample interaction can be modeled, the geometry of each individual probe is subtly different (especially the tip) and that it changes during the probe usage.

With the success of the modeling results notwithstanding, the main barrier to effectively measuring the optical constants of materials is still the lack of an effective calibration method that will remove the contributions to the signal, which are dependent on the probe geometry and the rest of the s-SNOM system. The conventional baseline subtraction approach is not effective enough to address these problems.

In this Letter, we propose a method for measuring the optical constants of materials, which takes into account the essential

electromagnetic interactions that underpin the probe-sample coupling and incorporates them effectively in our calibration process. The method requires no prior knowledge of the model of the optical constants of the sample, nor the geometry of the probe. The vector nature of the calibration method, akin to those used in microwave measurements, is the key to properly removing the spurious contributions to the scattering signal and the extraction of both the real and the imaginary parts of the complex optical constants of materials.

In order to demonstrate our method, we extracted the optical properties of several materials with optical constants known with high accuracy and those of differently doped regions of a standard Silicon RAM (SRAM) sample using a THz s-SNOM in the range of 0.6–1.0 THz. While we employed a THz TDS system in our experiments, the proposed calibration method is source agnostic and translates readily to other sources including electronic THz sources,[35] QCL-based systems,[36–38] and sources at other than THz wavelengths including MIR, near-infrared, or visible parts of the spectrum.

Figure 1(a) depicts diagrammatically the interaction of the incident THz wave (with the field E_{inc}) with the probe-sample pair and the formation of the resulting scattered wave with the field E_{scat}. This process is at the core of the s-SNOM operation. The field E_{scat} containing the information about the sample can be related to E_{inc} via the scattering coefficient σ,[31]

$$\sigma(\omega) = E_{scat}(\omega)/E_{inc}(\omega). \qquad (1)$$

The model for $\sigma(\omega)$ is built on the premise that the electric dipole is formed in the tip illuminated by the incident field E_{inc}.[39] The dipole charge located in the apex of the probe (close to the sample) creates its mirror image, thus forming a secondary dipole—mirror dipole—in the sample. The mirror dipole acts back on the probe increasing further its polarization. This, in turn, increases the mirror dipole moment. Multiple interactions between the tip and the mirror dipoles, in a self-consistent manner, define the total charge located at the tip in the presence of a sample and, therefore, the effective dipole moment.[40–42] The resulting scattering coefficient is proportional to[39]

$$\sigma(\omega) \propto 1 + \frac{\frac{f_0}{2}\beta}{1 - f_1\beta}, \qquad (2)$$

where β is the quasi-static reflection coefficient and f_0 and f_1 are the probe geometric response factors.[42] The recursive nature of the process
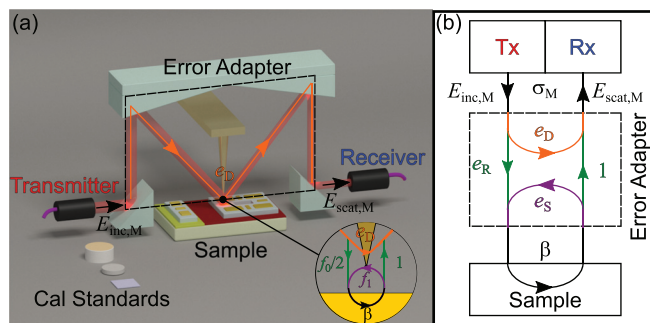

FIG. 1. (a) s-SNOM configuration: a schematic representation and (b) Flow diagram of the error adapter.

that leads to the formation of the total dipole moment through multiple interactions between the tip and the sample [as seen from the second term in (2)] creates a situation akin to that of multiple reflections within an optical resonator or multiple reflections between the microwave source and the load connected via a transmission line. Not surprisingly, for both the above-mentioned systems, scattering coefficients can be modeled by an expression suggestive of an iterative process or a feedback loop: they can be modeled by a loop being formed between the two elements in the system. Therefore, the scattering coefficient is not directly proportional to the sample's reflection coefficient: the material response is embedded in the loop described by (2). This obviously complicates the process of extracting the optical constants of the sample from s-SNOM measurements. A similar situation has been dealt with in microwave network analyzers (VNAs) by identifying non-idealities of the measurement system and attributing them to a virtual "error adapter" external to, and separated from, the idealized measurement system.[43,44]

The finite dipole model suggests that similar analysis can be applied to s-SNOM to address complex issues inherent to its calibration and that these non-idealities can be represented by the adapter shown in Fig. 1(b).

In particular, the adapter addresses

(1) Reflections from the oscillating parts of the measurement system including the cantilever and the absorption and the delay along the pathways from the transmitting antenna to the cantilever and back to the receiver antenna. This can be attributed to the term called, following the VNA nomenclature, the directivity error e_D. It includes the sample-agnostic contributions to the response signal.
(2) The spectral dependence of the source and the spectral response of the probe-sample pair that we will include in the reflection tracking element e_R.
(3) The multiple interactions between the tip and the sample, adequately described in the finite dipole model by the iterative build-up of the secondary dipole moments, will be included in the term called source match error e_S.

Therefore, the realistic s-SNOM model can now be described by a combination of an idealized s-SNOM system and the "far-field to near-field adapter," which describes the interaction between the s-SNOM system and the sample under test.

In the remainder of this Letter, we will describe the process of extracting the values of three unknown terms of the adapter (e_D, e_R, and e_S) and the process of calibrating the system.

Based on the adapter flow diagram in Fig. 1(b), the relationship between the measured scattering coefficient $\sigma_M(\omega)$ and the actual, electrostatic reflection coefficient of the sample $\beta(\omega)$ is given by[43,44]

$$\sigma_M(\omega) = e_D(\omega) + \frac{e_R(\omega)\beta(\omega)}{1 - e_S(\omega)\beta(\omega)}, \qquad (3)$$

an equation identical in form to the VNA error adapter, suggesting that a similar calibration process can be used for both systems. Therefore, the striking similarity between (2) and (3) is the key to the success of the proposed scheme.

To calibrate the system, one needs to measure three materials (standards) with known $\beta(\omega)$ coefficients at all frequencies in the required measurement range. This provides measured values for

$\sigma_{M,i}(\omega)$ for $i = 1, 2, 3$. Three known $\beta_i(\omega)$ values give three equations for e_D, e_R, and e_S. By solving these three equations, we obtain the error terms e_D, e_R, and e_S.[43]

Provided that the optical dielectric constants, $\epsilon(\omega)$, of the three standards are known from either measurements or the model, $\beta_i(\omega)$ of the standards can be calculated from $\beta(\omega) = (\epsilon(\omega) - 1)/(\epsilon(\omega) + 1)$.[31] Once the error terms have been extracted, it is straightforward to obtain $\beta(\omega)$ from the measured $\sigma_M(\omega)$,

$$\beta(\omega) = \frac{\sigma_M(\omega) - e_D(\omega)}{(\sigma_M(\omega) - e_D(\omega))e_S(\omega) + e_R(\omega)}, \qquad (4)$$

and the corresponding $\epsilon(\omega)$ of the material under test.

The following standards were used to calibrate the system: (1) a standard unprotected gold (Au) mirror (Thorlabs, PF05–03-M03) with $\epsilon_{Au}(\omega)$ values calculated using.[45] (2) a diced silicon (Si) substrate (ProSciTech, GA540–10) commonly used as an AFM mount, with a DC resistivity of $\sim 22\,\Omega \cdot cm$ and $\epsilon_{Si}(\omega)$ simulated using the model from Refs. 46 and 47 (3) finally, air was measured with the probe tapping in free space (with no sample/substrate below) and assuming the ideal value $\epsilon_{Air}(\omega) = 1 - j0$. These permittivity values were converted into $\beta_i(\omega)$. The s-SNOM system used was a NeaSNOM, Neaspec, with a THz TDS source (MenloSystems, TeraSmart), utilizing a commercial AFM tip (Rocky Mountain: 25PtIr200B-H, length 80 μm, and tip radius 45 nm). The geometry of an AFM tip varies markedly between the individual tips and the particular tip used in this study, which had a usable bandwidth of 0.6–1.0 THz and a spatial resolution

of $\sim$150 nm using a tapping amplitude of 300 nm. An integration time of 500 ms and a delay distance of 10 ps were used for the spectroscopy measurements, which were carried out in an un-purged atmosphere at the temperature of $23.5 \pm 0.5\,°C$ with a relative humidity of $53 \pm 2\%$.

To evaluate the system and the effectiveness of the calibration method, two different sample types were explored.

First, several materials with optical constants known with high accuracy were measured: (a) High-Resistivity Float Zone Silicon (HRFZ-Si) wafer (Tydex BS-HRFZ-SI-D50.8-T5, DC Resistivity $\sim$240 k$\Omega \cdot$ cm),[48] (b) standard BK7 glass microscope slide, (c) Tsurupica (picarin) window (Broadband,Inc., Tsurupica-RR-PP-25–2 mm), and (d) TPX window (Tydex, W-BAF2-D25-T2).

Second, a sample whose optical properties vary spatially on the micrometer scale was investigated: we used a standard SRAM sample (Bruker Nano Inc, SCM Test Sample).[49]

Let us first have a look at the effect of the calibration on the reflectivity spectrum. Figures 2(a) and 2(b) show the amplitude and phase, respectively, of the uncalibrated scattering signal's second harmonic captured by the NeaSNOM, a quantity proportional to the complex scattering coefficient of the sample and used as $\sigma_M(\omega)$.

Figures 2(c) and 2(d) show the magnitude and phase of the far-field complex reflectivity of the sample after the calibration [calculated from the extracted $\epsilon(\omega)$].

The results are comparable to those obtained using conventional far-field systems[50–52] (for details, see Table I). The comparison between the response before and after the calibration is striking: the
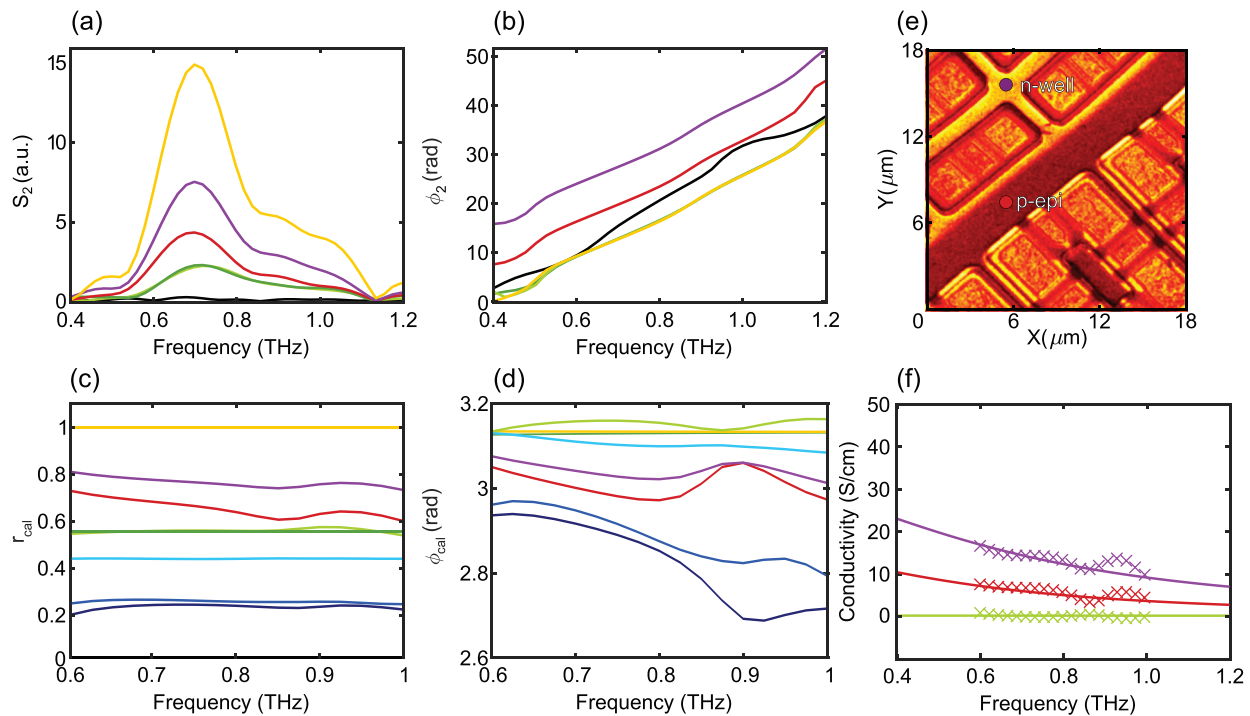
FIG. 2. Experimental results illustrating the proposed calibration scheme [colors indicate n-well (purple) and p-epi (red), HRFZ-Si (lime), BK7 (light blue), Tsurupica (blue), TPX (dark blue), Au (Cal) (gold), Si substrate (Cal) (green), and Air (Cal) (black)]. (a) Measured second harmonic near-field amplitude (uncalibrated reflectivity). (b) Measured second harmonic near-field phase (uncalibrated phase). (c) Calibrated reflectivity. (d) Calibrated phase (Air not in range presented). (e) THz s-SNOM image for the SRAM showing the location n-well and p-epi doped regions. (f) Extracted conductivity for SRAM via s-SNOM (markers) and fitted by the Drude model (solid lines).

TABLE I. Literature[50–52] vs Extracted n.

Material	n Literature value	n Extracted value
HRFZ-Si	3.41	3.39 ± 0.02
BK7	2.5	2.5 ± 0.01
Tsurupica	1.53	1.55 ± 0.02
TPX	1.47	1.49 ± 0.03

spectral features of the source and the system are dominating as shown in Fig. 2(a), where the calibrated response shown in Fig. 2(c) displays the corrected, virtually flat reflectivity across the measured frequency range. The error-corrected phase plots demonstrate that the propagation delay in free space has been properly removed in the calibration process [compare Figs. 2(b) and 2(d)].

The refractive indices of HRFZ-Si, BK7, Tsurupica, and TPX are known with high accuracy and are practically constant in the frequency range used in this study; our measurements on these materials agree extremely well with the published results (see Table I).

Figure 2(e) shows the THz image obtained using the NeaSNOM software, with clear contrast between differently doped regions matching well with what is reported in the literature.[35] This image was used to decide where on the SRAM, the THz spectroscopy would be carried out.

The conductivities of the differently doped regions (as well as for the HRFZ-Si) were calculated directly from our measurement after calibration [shown in Fig. 2(f) as markers]. The Drude model [shown in Fig. 2(f) as solid lines] was fitted to the data, and the carrier concentrations were extracted from the model (results are shown in Table II). The concentrations extracted for p-epi and n-well regions agree with the values provided in the SRAM datasheet[49] and in the literature.[24]

One of the more interesting results is the conductivity of the HRFZ-Si. For the high-resistivity silicon, we expected the conductivity of a few $\mu S \cdot cm^{-1}$ (estimated from the DC resistivity). However, the conductivity calculated from our measurements appears to be much higher 0.29 ± 1.3 mS $\cdot cm^{-1}$ (from our Drude model fit, we estimate the DC Resistivity at $\sim 20\, k\Omega \cdot cm$) [see Fig. 2(f)]. While the relative difference appears to be significant, the absolute error is smaller than 1 mS. This material is almost lossless; the reflection phase is close to π, and the small uncertainties in the measured phase (at the detection limit of the system and potentially caused by the temporal environmental changes occurring between the calibration time and the measurement time) are translated to significant relative error in the extracted conductivity. The same holds for other lossless materials. A configuration where the calibration standards are adjacent to the sample and are measured almost concurrently may be conducive to minimizing these issues.

TABLE II. Design values for carrier concentrations[48,49] and the measured values.

Material	Datasheet value (cm^{-3})	Measured value (cm^{-3})
n-well	2×10^{17}	1.56×10^{17}
p-epi	2×10^{16}	4.64×10^{16}
HRFZ-Si	1.8×10^{10}	2×10^{11}

The calibration method presented here allows for the fitting-free extraction of optical constants from s-SNOM spectral measurements, thus markedly enhancing the capability of the s-SNOM technique. The vector nature of the calibration method allows one to extract complex optical constants without the need for prior electromagnetic modeling of the probe-sample interactions, nor the knowledge of the probe geometry. The accuracy of the extracted optical constants is comparable to those obtained using conventional far-field techniques while additionally allowing for the characterization of their spatial distribution at the nanoscale, including the investigation of nanoparticles and nanowires. The source-independent nature of the proposed technique makes it directly applicable for s-SNOM measurements in other spectral ranges.

DATA AVAILABILITY

The data that support the findings of this study are available from the corresponding author upon reasonable request.

REFERENCES

[1]E. Synge, "XXXVIII. a suggested method for extending microscopic resolution into the ultra-microscopic region," London, Edinburgh Dublin Philos. Mag. J. Sci. **6**, 356–362 (1928).

[2]E. Ash and G. Nicholls, "Super-resolution aperture scanning microscope," Nature **237**, 510 (1972).

[3]F. Zenhausern, Y. Martin, and H. Wickramasinghe, "Scanning interferometric apertureless microscopy: Optical imaging at 10 angstrom resolution," Science **269**, 1083–1085 (1995).

[4]R. Hillenbrand, T. Taubner, and F. Keilmann, "Phonon-enhanced light–matter interaction at the nanometre scale," Nature **418**, 159 (2002).

[5]T. Taubner, R. Hillenbrand, and F. Keilmann, "Nanoscale polymer recognition by spectral signature in scattering infrared near-field microscopy," Appl. Phys. Lett. **85**, 5064–5066 (2004).

[6]F. Keilmann, A. J. Huber, and R. Hillenbrand, "Nanoscale conductivity contrast by scattering-type near-field optical microscopy in the visible, infrared and THz domains," J. Infrared, Millimeter, Terahertz Waves **30**, 1255–1268 (2009).

[7]S. Amarie, P. Zaslansky, Y. Kajihara, E. Griesshaber, W. W. Schmahl, and F. Keilmann, "Nano-FTIR chemical mapping of minerals in biological materials," Beilstein J. Nanotechnol. **3**, 312–323 (2012).

[8]K. Bulat, A. Rygula, E. Szafraniec, Y. Ozaki, and M. Baranska, "Live endothelial cells imaged by scanning near-field optical microscopy (SNOM): capabilities and challenges," J. Biophotonics **10**, 928–938 (2017).

[9]I. Amenabar, S. Poly, M. Goikoetxea, W. Nuansing, P. Lasch, and R. Hillenbrand, "Hyperspectral infrared nanoimaging of organic samples based on Fourier transform infrared nanospectroscopy," Nat. Commun. **8**, 14402 (2017).

[10]A. Cernescu, M. Szuwarzyński, U. Kwolek, P. Wydro, M. Kepczynski, S. Zapotoczny, M. Nowakowska, and L. Quaroni, "Label-free infrared spectroscopy and imaging of single phospholipid bilayers with nanoscale resolution," Anal. Chem. **90**, 10179–10186 (2018).

[11]X. Chen, D. Hu, R. Mescall, G. You, D. Basov, Q. Dai, and M. Liu, "Modern scattering-type scanning near-field optical microscopy for advanced material research," Adv. Mater. **31**, 1804774 (2019).

[12]S. G. Stanciu, D. E. Tranca, L. Pastorino, S. Boi, Y. M. Song, Y. J. Yoo, S. Ishii, R. Hristu, F. Yang, G. Bussetti, and G. A. Stanciu, "Characterization of nanomaterials by locally determining their complex permittivity with scattering-type scanning near field optical microscopy," ACS Appl. Nano Mater. **3**, 1250 (2020).

[13]H.-T. Chen, R. Kersting, and G. C. Cho, "Terahertz imaging with nanometer resolution," Appl. Phys. Lett. **83**, 3009–3011 (2003).

[14]H.-G. von Ribbeck, M. Brehm, D. van der Weide, S. Winnerl, O. Drachenko, M. Helm, and F. Keilmann, "Spectroscopic THz near-field microscope," Opt. Express **16**, 3430–3438 (2008).

[15]F. Huth, M. Schnell, J. Wittborn, N. Ocelic, and R. Hillenbrand, "Infrared-spectroscopic nanoimaging with a thermal source," Nat. Mater. **10**, 352–356 (2011).

[16]K. Moon, Y. Do, M. Lim, G. Lee, H. Kang, K.-S. Park, and H. Han, "Quantitative coherent scattering spectra in apertureless terahertz pulse near-field microscopes," Appl. Phys. Lett. **101**, 011109 (2012).

[17]F. Kuschewski, H.-G. von Ribbeck, J. Döring, S. Winnerl, L. Eng, and S. Kehr, "Narrow-band near-field nanoscopy in the spectral range from 1.3 to 8.5 THz," Appl. Phys. Lett. **108**, 113102 (2016).

[18]S. Amarie and F. Keilmann, "Broadband-infrared assessment of phonon resonance in scattering-type near-field microscopy," Phys. Rev. B **83**, 045404 (2011).

[19]L. Wehmeier, T. Nörenberg, T. V. de Oliveira, J. M. Klopf, S.-Y. Yang, L. W. Martin, R. Ramesh, L. M. Eng, and S. C. Kehr, "Phonon-induced near-field resonances in multiferroic $BiFeO_3$ thin films at infrared and THz wavelengths," Appl. Phys. Lett. **116**, 071103 (2020).

[20]X. Chen, J. Zhang, Z. Yao, H. A. Bechtel, M. C. Martin, G. Carr, and M. Liu, "Ultrabroadband infrared near-field spectroscopy and imaging of local resonators in percolative gold films," J. Opt. Soc. Am. B **36**, 3315–3321 (2019).

[21]J. Stiegler, A. Huber, S. L. Diedenhofen, J. Gomez Rivas, E. Algra, E. Bakkers, and R. Hillenbrand, "Nanoscale free-carrier profiling of individual semiconductor nanowires by infrared near-field nanoscopy," Nano Lett. **10**, 1387–1392 (2010).

[22]L. Jung, J. Pries, T. W. Maß, M. Lewin, D. S. Boyuk, A. T. Mohabir, M. A. Filler, M. Wuttig, and T. Taubner, "Quantification of carrier density gradients along axially-doped silicon nanowires using infrared nanoscopy," ACS Photonics **6**, 1744 (2019).

[23]A. J. Huber, F. Keilmann, J. Wittborn, J. Aizpurua, and R. Hillenbrand, "Terahertz near-field nanoscopy of mobile carriers in single semiconductor nanodevices," Nano Lett. **8**, 3766–3770 (2008).

[24]N. A. Aghamiri, F. Huth, A. J. Huber, A. Fali, R. Hillenbrand, and Y. Abate, "Hyperspectral time-domain terahertz nano-imaging," Opt. Express **27**, 24231–24242 (2019).

[25]A. A. Govyadinov, I. Amenabar, F. Huth, P. S. Carney, and R. Hillenbrand, "Quantitative measurement of local infrared absorption and dielectric function with tip-enhanced near-field microscopy," J. Phys. Chem. Lett. **4**, 1526–1531 (2013).

[26]A. A. Govyadinov, S. Mastel, F. Golmar, A. Chuvilin, P. S. Carney, and R. Hillenbrand, "Recovery of permittivity and depth from near-field data as a step toward infrared nanotomography," ACS Nano **8**, 6911–6921 (2014).

[27]A. S. McLeod, P. Kelly, M. Goldflam, Z. Gainsforth, A. J. Westphal, G. Dominguez, M. H. Thiemens, M. M. Fogler, and D. Basov, "Model for quantitative tip-enhanced spectroscopy and the extraction of nanoscale-resolved optical constants," Phys. Rev. B **90**, 085136 (2014).

[28]F. Mooshammer, F. Sandner, M. A. Huber, M. Zizlsperger, H. Weigand, M. Plankl, C. Weyrich, M. Lanius, J. Kampmeier, G. Mussler, D. Grützmacher, J. L. Boland, T. L. Cocker, and R. Huber, "Nanoscale near-field tomography of surface states on $(Bi_{0.5}Sb_{0.5})2Te_3$," Nano Lett. **18**, 7515–7523 (2018).

[29]K. Moon, Y. Do, H. Park, J. Kim, H. Kang, G. Lee, J.-H. Lim, J.-W. Kim, and H. Han, "Computed terahertz near-field mapping of molecular resonances of lactose stereo-isomer impurities with sub-attomole sensitivity," Sci. Rep. **9**, 16915 (2019).

[30]B. Knoll and F. Keilmann, "Enhanced dielectric contrast in scattering-type scanning near-field optical microscopy," Opt. Commun. **182**, 321–328 (2000).

[31]A. Cvitković, N. Ocelić, and R. Hillenbrand, "Analytical model for quantitative prediction of material contrasts in scattering-type near-field optical microscopy," Opt. Express **15**, 8550–8565 (2007).

[32]B.-Y. Jiang, L. Zhang, A. Castro Neto, D. Basov, and M. Fogler, "Generalized spectral method for near-field optical microscopy," J. Appl. Phys. **119**, 054305 (2016).

[33]S. Chui, X. Chen, M. Liu, Z. Lin, and J. Zi, "Scattering of electromagnetic waves from a cone with conformal mapping: Application to scanning near-field optical microscope," Phys. Rev. B **97**, 081406 (2018).

[34]F. L. Ruta, A. J. Sternbach, A. B. Dieng, A. S. McLeod, and D. N. Basov, "Quantitative nano-infrared spectroscopy of anisotropic van der Waals materials," Nano Lett. **20**, 7933 (2020).

[35]C. Liewald, S. Mastel, J. Hesler, A. J. Huber, R. Hillenbrand, and F. Keilmann, "All-electronic terahertz nanoscopy," Optica **5**, 159–163 (2018).

[36]P. Dean, O. Mitrofanov, J. Keeley, I. Kundu, L. Li, E. H. Linfield, and A. G. Davies, "Apertureless near-field terahertz imaging using the self-mixing effect in a quantum cascade laser," Appl. Phys. Lett. **108**, 091113 (2016).

[37]M. C. Giordano, S. Mastel, C. Liewald, L. L. Columbo, M. Brambilla, L. Viti, A. Politano, K. Zhang, L. Li, A. G. Davies, E. H. Linfield, R. Hillenbrand, F. Keilmann, G. Scamarcio, and M. S. Vitiello, "Phase-resolved terahertz self-detection near-field microscopy," Opt. Express **26**, 18423–18435 (2018).

[38]A. Rakić, T. Taimre, K. Bertling, Y. Lim, P. Dean, A. Valavanis, and D. Indjin, "Sensing and imaging using laser feedback interferometry with quantum cascade lasers," Appl. Phys. Rev. **6**, 021320 (2019).

[39]L. Mester, A. A. Govyadinov, S. Chen, M. Goikoetxea, and R. Hillenbrand, "Subsurface chemical nanoidentification by nano-FTIR spectroscopy," Nat. Commun. **11**, 3359 (2020).

[40]F. Keilmann and R. Hillenbrand, "Near-field microscopy by elastic light scattering from a tip," Philos. Trans. R. Soc. A **362**, 787–805 (2004).

[41]J. Aizpurua, T. Taubner, F. J. G. de Abajo, M. Brehm, and R. Hillenbrand, "Substrate-enhanced infrared near-field spectroscopy," Opt. Express **16**, 1529–1545 (2008).

[42]A. Cvitković, "Substrate-enhanced scattering-type scanning near-field infrared microscopy of nanoparticles," Ph.D. thesis (Technische Universität München, 2009).

[43]G. H. Bryant, *Principles of Microwave Measurements* (IET, 1993), Vol. 5.

[44]M. Hiebel, *Fundamentals of Vector Network Analysis* (Rohde & Schwarz, 2007).

[45]A. D. Rakić, A. B. Djurišić, J. M. Elazar, and M. L. Majewski, "Optical properties of metallic films for vertical-cavity optoelectronic devices," Appl. Opt. **37**, 5271–5283 (1998).

[46]G. Masetti, M. Severi, and S. Solmi, "Modeling of carrier mobility against carrier concentration in arsenic-, phosphorus-, and boron-doped silicon," IEEE Trans. Electron Devices **30**, 764–769 (1983).

[47]M. Van Exter and D. Grischkowsky, "Carrier dynamics of electrons and holes in moderately doped silicon," Phys. Rev. B **41**, 12140 (1990).

[48]Silicon Datasheet (Tydex, St.Peterburg, Russia, 2018), http://www.tydexoptics.com/materials1/for_transmission_optics/silicon/.

[49]The Bruker SCM Test Sample (Bruker AFM Probes, Camarillo, CA, USA, 2012), https://www.brukerafmprobes.com/p-3553-scmsample.aspx.

[50]M. Naftaly and R. E. Miles, "Terahertz time-domain spectroscopy for material characterization," Proc. IEEE **95**, 1658–1665 (2007).

[51]E. Fedulova, M. M. Nazarov, A. Angeluts, M. Kitai, V. Sokolov, and A. Shkurinov, "Studying of dielectric properties of polymers in the terahertz frequency range," Proc. SPIE **8337**, 83370I (2012).

[52]J. Dai, J. Zhang, W. Zhang, and D. Grischkowsky, "Terahertz time-domain spectroscopy characterization of the far-infrared absorption and index of refraction of high-resistivity, float-zone silicon," J. Opt. Soc. Am. B **21**, 1379–1386 (2004).